



**HAL**  
open science

## Mesostructure - thermoelectric properties relationships in $V_xMn_{1-x}Si_{1.74}$ ( $x=0, 0.04$ ) higher manganese silicides prepared by magnesiothermy

Sylvain Le Tonquesse, Vincent Dorcet, Loïc Joanny, Valérie Demange,  
Carmelo Prestipino, Quansheng Guo, David Berthebaud, Takao Mori,  
Mathieu Pasturel

### ► To cite this version:

Sylvain Le Tonquesse, Vincent Dorcet, Loïc Joanny, Valérie Demange, Carmelo Prestipino, et al.. Mesostructure - thermoelectric properties relationships in  $V_xMn_{1-x}Si_{1.74}$  ( $x=0, 0.04$ ) higher manganese silicides prepared by magnesiothermy. *Journal of Alloys and Compounds*, 2020, 816, pp.152577. 10.1016/j.jallcom.2019.152577 . hal-02470151

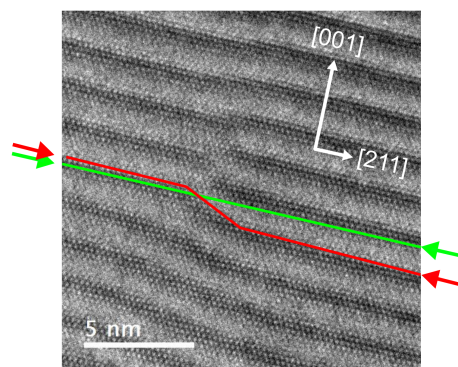
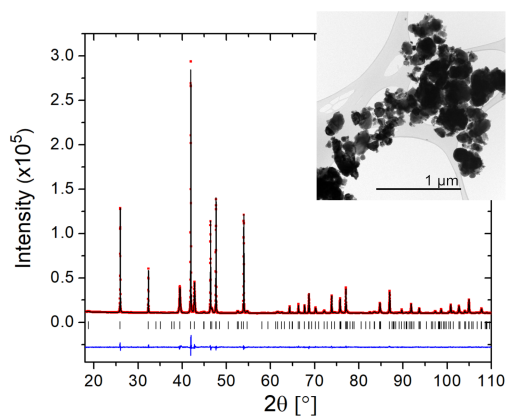
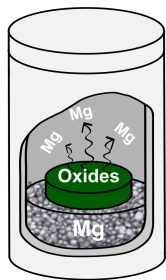
**HAL Id: hal-02470151**

**<https://univ-rennes.hal.science/hal-02470151>**

Submitted on 11 Feb 2020

**HAL** is a multi-disciplinary open access archive for the deposit and dissemination of scientific research documents, whether they are published or not. The documents may come from teaching and research institutions in France or abroad, or from public or private research centers.

L'archive ouverte pluridisciplinaire **HAL**, est destinée au dépôt et à la diffusion de documents scientifiques de niveau recherche, publiés ou non, émanant des établissements d'enseignement et de recherche français ou étrangers, des laboratoires publics ou privés.



Journal Pre-proof

# Mesostructure - thermoelectric properties relationships in $V_xMn_{1-x}Si_{1.74}$ ( $x = 0, 0.04$ ) Higher Manganese Silicides prepared by magnesiothermy

Sylvain Le Tonquesse<sup>a</sup>, Vincent Dorcet<sup>a</sup>, Loic Joanny<sup>a</sup>, Valérie Demange<sup>a</sup>,  
Carmelo Prestipino<sup>a</sup>, Quansheng Guo<sup>b</sup>, David Berthebaud<sup>b</sup>, Takao Mori<sup>c</sup>,  
Mathieu Pasturel<sup>a</sup>

<sup>a</sup>Univ Rennes, CNRS, ISCR-UMR6226/ScanMAT-UMS2001, F-35000, Rennes, France

<sup>b</sup>CNRS - Saint-Gobain - NIMS, UMI3629, Laboratory for Innovative Key Materials and Structures (LINK), National Institute for Materials Science, 1-1 Namiki, Tsukuba, Ibaraki 305-0044, Japan

<sup>c</sup>National Institute for Materials Science (NIMS), WPI-MANA and CFSN, Tsukuba, Japan

---

## Abstract

The synthesis of pure pristine and vanadium-doped  $MnSi_\gamma$  ( $\gamma = 1.74$ ) powder by a relatively fast, 'low temperature' and high yield magnesiothermy process is described. The powder obtained by this innovative route is composed of well crystallized grains with sizes ranging from 20 to 500 nm and free from any  $MnSi$  precipitates. Mesostructured densified pellets with average grain sizes as small as 550 nm are obtained by spark plasma sintering (SPS). Detailed structural and microstructural characterization of the samples were realized at every stage of the process, highlighting a high concentration of defects such as orientational or spacing anomalies of the Nowotny phase,  $\gamma$  variations within a single grain and dislocations. Accordingly a significant decrease of the lattice thermal conductivity is evidenced in comparison to conventionally synthesized (arc-melting/SPS) samples having similar density and (V/)Mn/Si stoichiometry. The thermoelectric properties of these materials are discussed in regard of their complex microstructure.

**Keywords:** Intermetallics, thermoelectric materials, chemical synthesis, crystal structure, transmission electron microscopy

---

\*mathieu.pasturel@univ-rennes1.fr

## 1. Introduction

Thermoelectric (TE) materials are being extensively investigated for their potential of energy-saving and dynamical energy harvesting through solid state conversion of heat into electricity [1, 2]. Higher Manganese Silicides (HMS) with chemical formula  $\text{MnSi}_\gamma$  ( $1.72 < \gamma < 1.75$ ) are widely considered as a promising thermoelectrical material because of their potential in industrial application. Indeed, HMS are low density materials composed of non-hazardous and inexpensive elements and they possess very good mechanical properties and oxidation resistance. HMS are currently used as *p*-type material for industrial thermoelectric generator (TEG) prototypes operating at mid-temperature [3, 4]. However, a large scale industrial implementation of such materials is limited by their moderate thermoelectric properties usually evaluated by the figure-of-merit  $ZT$  defined as:

$$ZT = \frac{\alpha^2}{\rho(\kappa_L + \kappa_e)} T \quad (1)$$

where  $\alpha$  is the Seebeck coefficient,  $\rho$  the electrical resistivity,  $\kappa_L$  and  $\kappa_e$  the lattice and electronic contribution to the total thermal conductivity  $\kappa$  and  $T$  the operating temperature.

Improvement of their TE properties can be achieved through various strategies enhancing  $ZT$  [5, 6]. Many studies have been focused on chemical doping of  $\text{MnSi}_\gamma$  to increase the power factor  $PF = \alpha^2/\rho$  [7, 8] or on fabrication of elaborated microstructures with the aim to decrease  $\kappa_L$  via synthesis routes such as ball-milling [9], melt-spinning [10, 11], fast combustion [12] or reactive sintering [13, 14]. For example,  $ZT_{max}$  exceeding unity has been obtained for Re supersaturated HMS realized by liquid quenching [15, 16] at the expense of industrial scalability and elevated price of Re.

Investigation of HMS is rather difficult because these materials are characterized by a high structural, microstructural and synthesis complexity. This

28 includes (i) the difficulty to obtain pure samples due to the incongruent melt-  
29 ing of  $\text{MnSi}_\gamma$  [17] and the high vapor pressure of Mn at elevated temperature  
30 [18], (ii) the formation of metallic MnSi precipitates inside HMS grains which  
31 can severely affect the TE [19, 20] and mechanical [21] properties, (iii) the  
32 incommensurate chimney-ladder crystal structure which is often unsatisfacto-  
33 rily described as a series of commensurate  $\text{Mn}_y\text{Si}_x$  structures ( $x, y$  are natural  
34 numbers) [22], and (iv) the anisotropic transport properties which can bias the  
35 comparison of performances in the case of crystallographically textured samples  
36 [23].

37 Recently, we reported on the synthesis of high purity mesostructured TE  
38 skutterudites by magnesio-reduction of oxides [24]. This scalable process based  
39 on cheap and air-stable oxides leads to the formation at moderate temperature  
40 of well crystallized submicronic powders with elevated TE properties. Simi-  
41 lar process was attempted to obtain HMS powders by Girard *et al.* [25] starting  
42 from nanosilica and  $\text{MnO}_2$  in molten salt fluxes but the information on such pro-  
43 cess is limited to a single conference abstract and, to the best of our knowledge,  
44 no peer-review article has ever been published. We have thus applied a flux-free  
45 magnesio-reduction process employing MnO and Si as reactants for the synthesis  
46 of pure and vanadium doped  $\text{MnSi}_{1.74}$ . The structural and microstructural char-  
47 acterizations, using X-ray diffraction Rietveld refinements in a composite crystal  
48 structure model, electron backscattering diffraction and scanning/transmission  
49 electron microscopy on both as-synthesized powders and spark plasma sintered  
50 pellets are presented thereafter. The thermal dependence of the electrical resis-  
51 tivity, Seebeck coefficient and thermal conductivity have been measured in the  
52 temperature range 300-800 K and subsequent thermoelectric performances are  
53 discussed in terms of structure-microstructure-properties relationships. These  
54 results are compared to equivalent HMS prepared by conventional melting-  
55 solidification-annealing method.

## 2. Experimental procedure

For the magnesio-reduction (MR) synthesis of  $\text{MnSi}_{1.74}$  and  $\text{V}_{0.04}\text{Mn}_{0.96}\text{Si}_{1.74}$ , precursor mixtures first need to be prepared by ball-milling of  $\text{V}_2\text{O}_5$  (Merck, 99 %),  $\text{MnO}$  (Alfa Aesar, 99 %) and  $\text{Si}$  (Ventron, 99.9 %) with a molar ratio of 0 : 1 : 1.74 and 0.02 : 0.96 : 1.74, respectively, under air in a planetary mill (Retsch PM100) for 3 h at 650 rpm in a WC vial filled with  $\varnothing$  10 mm WC balls (fig. 1a). A small ball-to-powder ratio of 5 : 1 is used in order to avoid contamination by WC during the milling process. The obtained precursor mixture is cold-pressed at 65 MPa into  $\varnothing$  10 mm pellets with about 4 mm height. Each pellet is placed in a Mo-crucible with Mg turnings (Strem Chemicals,  $\geq$  99 %) equally distributed under and on top of the pellet (fig. 1b). Such distribution of Mg helps to maximize the surface contact between Mg and the pellets in order to promote a homogeneous reduction and was found compulsory to avoid the presence of  $\text{Mg}_2\text{Si}$  by-product. A 25 % excess Mg is empirically needed to complete the magnesio-reduction reaction:



A graphite seal is inserted between the crucible and the lid and the system is held tight with a clamping system. This set-up is placed in an Inconel tube filled with Ar to avoid the Mo-crucible oxidization. The whole is heated up to 1173 K at a rate of  $60 \text{ K h}^{-1}$  in a tubular furnace and held at this temperature for 8 h before being cooled down by switching off the furnace (fig. 1c). At the end of the reaction the product still in the shape of a pellet can be easily separated from loose MgO powder (fig. 1d). A black powder composed of  $\text{MnSi}_\gamma$  is obtained by softly crushing the pellet in an agate mortar. The MgO by-product is removed by soaking the as-synthesized powder twice in diluted hydrochloric acid (2 wt.%) for 5 - 10 minutes and washing three times with distilled water and once more with ethanol before being dried at 353 K overnight (fig. 1e). The washed  $\text{MnSi}_\gamma$

83 powder is then densified by spark plasma sintering (SPS) in  $\varnothing$  10 mm graphite  
 84 dies at 1273 K and 75 MPa for 20 min with  $100 \text{ K min}^{-1}$  heating/cooling rates  
 85 using a FCT HP-D-10 apparatus.

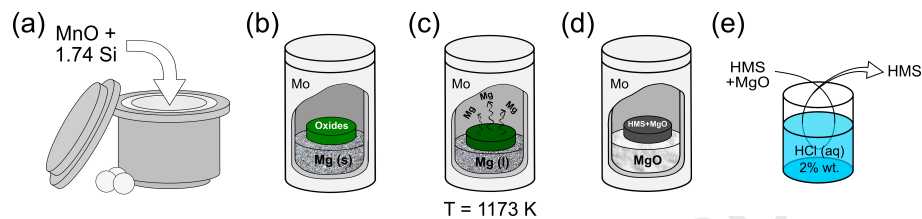


Figure 1: Main steps of the magnesio-reduction synthesis: (a) MnO and Si are ball-milled in WC vial; (b) pellets of MnO/Si mixture are sealed with the adequate amount of Mg in a Mo crucible; (c) Mg vapor reduces the oxides during the heat treatment at 1173 K; (d) the reduction is completed after 8 h at 1173 K; (e) MgO is removed from the product by soaking the powder in diluted HCl.

86 In order to investigate how magnesiothermy synthetic route affects the final  
 87 thermoelectric properties,  $\text{MnSi}_{1.74}$  has also been synthesized by conventional  
 88 fusion solidification method. Stoichiometric amounts of the elements are arc-  
 89 melted (AM) three times to ensure homogenization and the obtained ingot was  
 90 annealed for 100 h at 1273 K in evacuated silica tubes. The annealed ingot  
 91 was finely ground in an agate mortar and the powder was densified by SPS in  
 92  $\varnothing$  10 mm graphite dies at 1238 K and 80 MPa for 5 min.

93 The crystal structure and purity of the samples were checked by powder X-  
 94 ray diffraction (PXRD) using a Bruker D8 Advance diffractometer in the Bragg-  
 95 Brentano geometry working with a monochromatized  $\text{Cu K}\alpha_1$  radiation ( $\lambda = 1.5406 \text{ \AA}$ )  
 96 and equipped with a LynxEye detector. Structural parameters were determined  
 97 by Rietveld refinement of the PXRD patterns using JANA2006 [26]. Scanning  
 98 electron microscopy (SEM) images, energy dispersive spectroscopy (EDS) and  
 99 electron backscattering diffraction (EBSD) were performed using a JEOL JSM  
 100 7100F microscope equipped with an Oxford EDS SDD X-Max spectrometer and  
 101 an EBSD HKL Advanced Nordlys Nano detector. TEM analyses were performed  
 102 on a JEOL 2100 LaB<sub>6</sub> instrument operating at 200 kV and equipped with an  
 103 Oxford EDS SDD 80 mm<sup>2</sup> spectrometer and high resolution Gatan US1000 and  
 104 Orius 200D cameras. Preparation of the powder samples for SEM analyses con-

105 sisted in their deposition on carbon tape followed by metallization with car-  
 106 bon. For transmission electron microscopy (TEM), a small amount of powder  
 107 was sonicated in absolute ethanol and deposited for drying on a carbon coated  
 108 copper grid. For EBSD and EDS analyses, densified pellets were consecutively  
 109 mirror polished with 320 down to 1200 grit SiC papers, diamond paste (3 and  
 110 1  $\mu\text{m}$ ) and colloidal silica. EBSD mappings were analyzed using the *Channel*  
 111 *5* software (HKL Technology). Thin foils of densified pellet for TEM analyses  
 112 were obtained by dimpling a 100  $\mu\text{m}$  thick pellet down to 10  $\mu\text{m}$  with diamond  
 113 paste (3 and 1  $\mu\text{m}$ ) followed by Ar-ion milling using a Fischione Ion Mill 1010  
 114 operating at 4.5 kV and 4.5 mA.

115 The thermal diffusivity (D) has been measured by the laser flash method on  
 116  $\varnothing$  10 mm and 2 mm thick samples coated with graphite using a Netzsch LFA 467  
 117 HyperFlash equipment under  $\text{N}_2$  atmosphere. The thermal conductivity could  
 118 be calculated by the  $\kappa = DC_p d$  relation with  $C_p$  the specific heat of the sample  
 119 determined thanks to a Netzsch Pyroceram reference sample and  $d$  the density  
 120 measured by the Archimede method. The Seebeck coefficient and electrical  
 121 resistivity were measured simultaneously on  $6 \times 2 \times 2$  mm bars using a ZEM3  
 122 device (ULVAC-RIKO Inc., Yokohama, Japan) under He atmosphere.

### 123 3. Results and discussion

#### 124 3.1. Magnesio-reduction synthesis

125 The XRD pattern of the precursor mixture obtained by high energy ball-milling  
 126 of MnO and Si is shown in fig. 2. Interestingly, MnSi and  $\text{MnSi}_7$  readily start  
 127 to form in the milling vial indicating the reduction of manganese. According to  
 128 the Ellingham diagram [27, 28] the reduction of MnO by Si :



129 is thermodynamically possible. The activation energy for this reaction is prob-

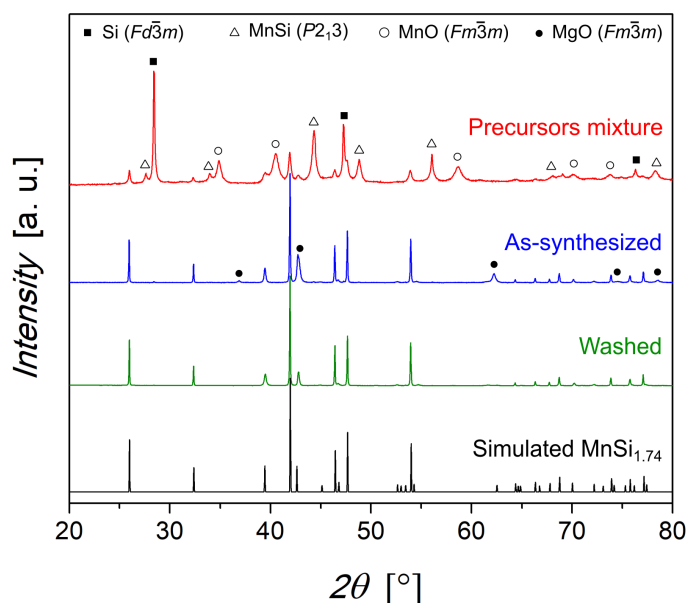
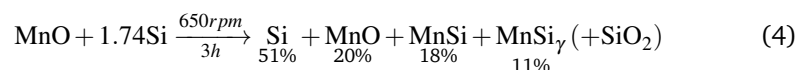


Figure 2: XRD patterns of the precursors mixture (red), as-synthesized HMS powder (blue), HCl washed HMS powder (green) and simulated pattern for  $\text{MnSi}_{1.74}$  with first order satellite peaks [22] (black). Some weak intensity satellite reflections in the simulated pattern might not be visible in the experimental ones because of their large broadening (see text for details).

ably overcome locally in the milling vial when highly energetic shocks occur.  
 Upon further milling, metallic Mn would then react with unreacted Si to form  
 $\text{MnSi}_\gamma$  and  $\text{MnSi}$  as already reported by different groups [29, 30, 31].  $\text{SiO}_2$  must  
 be present in the mixture but could not be detected by XRD due to its probable  
 amorphous nature. At the end of the milling step, a very intimate mixture of  
 Mn- and Si-containing species is produced according to:

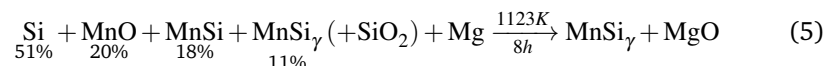


136

where the molar concentrations are determined from Rietveld refinement (see  
 fig. SI.1 and tables SI 1,2,3,4).

138

139 The precursors mixture is then reacted with Mg according to:



140

141 and XRD on the as-synthesized powders (fig. 2, blue curve) confirms that the  
142 product is only composed of MnSi<sub>γ</sub> and MgO.

143 Magnesio-reduction was attempted at several temperatures and a lower limit  
144 of 1073 K has been found to initiate this reaction. The high vapor pressure of Mg  
145 at these elevated temperatures is expected to easily penetrate inside the pellet  
146 to induce the reduction of the oxides and subsequent interdiffusion of native  
147 metals to form the targeted silicide. Additionally, the reduction of MnO and SiO<sub>2</sub>  
148 by Mg is highly exothermic at 1123 K with  $\Delta H_r = -346.9$  and  $-344.0$  kJ mol<sup>-1</sup>  
149 respectively [27, 28]. The heat released locally inside the pellet may accelerate  
150 the reaction and a scenario close to a combustion synthesis [32, 33] cannot be  
151 ruled out.

### 152 3.2. Microstructure of the magnesio-reduced MnSi<sub>γ</sub> powders

153 Fig. 3a and 3b show secondary electron SEM images of an as-synthesized MR  
154 HMS powder containing MnSi<sub>γ</sub> and MgO. It is composed of grains with sizes  
155 ranging from about 50 nm to several hundreds of nm, some of them forming  
156 aggregates with micrometric sizes. According to EDS elemental analyses, MgO  
157 constitute 60 at.% of the as-synthesized powder. Moreover, they give a Si/Mn  
158 metal ratio of about 1.7 which is in agreement with the targeted MnSi<sub>1.74</sub> com-  
159 position (fig. SI.2a).

160 The HMS + MgO composite microstructure has been investigated by TEM. A  
161 typical brightfield image of the as-synthesized HMS powder is shown in fig. 4a.  
162 EDS analyses and selected area electron diffraction realized on several areas of  
163 the sample assign the electron-opaque grains to MnSi<sub>γ</sub> while the more electron-  
164 transparent matrix is mainly composed of much smaller MgO crystals. These  
165 observations are consistent with the much broader XRD Bragg peaks ascribed

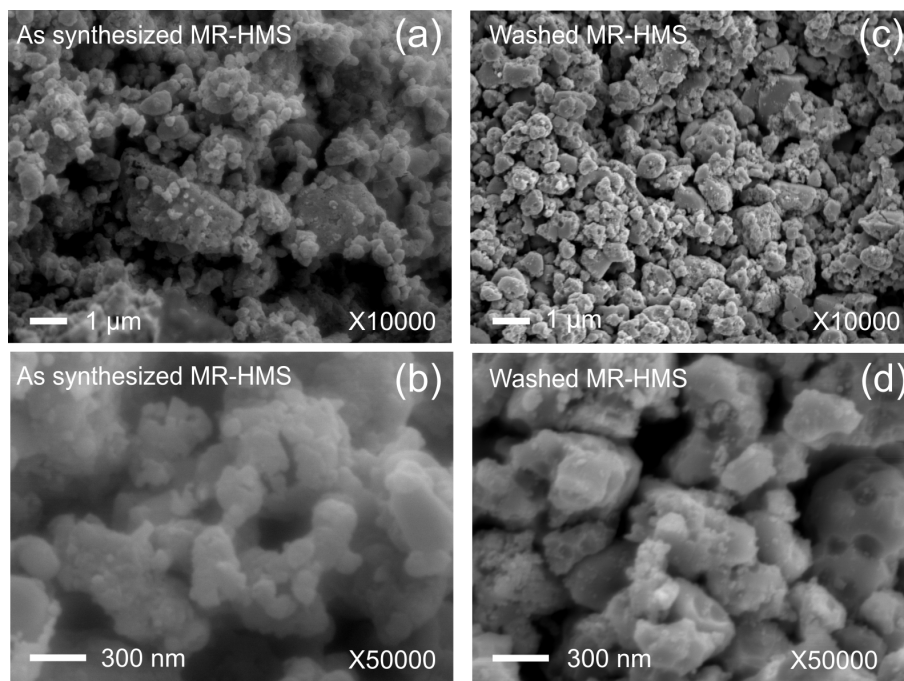


Figure 3: Secondary electron SEM images of (a)(b) as-synthesized MR HMS powder composed of  $\text{MnSi}_{1.74}$  and MgO and (c)(d) MR HMS powder after acidic washing containing only  $\text{MnSi}_{1.74}$ , at two different magnifications.

166 to MgO compared to those of HMS (fig. 2). We hypothesize here that the MgO  
 167 matrix formed during the MR reaction and surrounding the  $\text{MnSi}_y$  grains plays  
 168 a significant role by limiting the silicide particle growth at the rather elevated  
 169 reaction temperature and thus helps stabilizing the powder submicronic size.

170 After acidic washing, powder XRD (fig. 2) shows that MgO is eliminated,  
 171 at least down to the detection limit of the technique. The absence of Mg  $K_\alpha$   
 172 emission line on SEM-EDS analyses and the detection of only traces of Mg on  
 173 TEM-EDS confirm that MgO was almost entirely removed from the sample (fig.  
 174 SI.2). Without the surrounding MgO matrix, the morphology of the HMS grains  
 175 is fully revealed and typical SEM and TEM images are shown in fig. 3c,d and  
 176 4b, respectively. The grains have relatively isotropic shapes with sizes ranging  
 177 from about 50 to few hundreds of nm. Based on their relatively faceted shape,  
 178 most of the grains look single crystalline. Interestingly, high resolution trans-

179 mission electron microscopy (HRTEM) does not reveal any MnSi precipitates  
 180 inside the grains as is usually seen in samples obtained by crystallization from  
 181 a liquid melt. It should also be noticed that HRTEM observations of the sur-  
 182 face of the grains before and after the acidic washing (not shown here) do not  
 183 reveal any trace of chemical erosion of the grains by the acid. Electron diffrac-  
 184 tion patterns (fig. 4c) can be fully indexed using 4 Miller indices  $hk\ell m$  with the  
 185  $\text{MnSi}_\gamma$  composite crystal structure described in details in the next section. No-  
 186 ticeable orientation and spacing anomalies as already reported and described  
 187 by Ye and Amelinckx [34] are clearly visible along the  $[00\ell]$  rows and will be  
 188 further discussed in section 3.4.

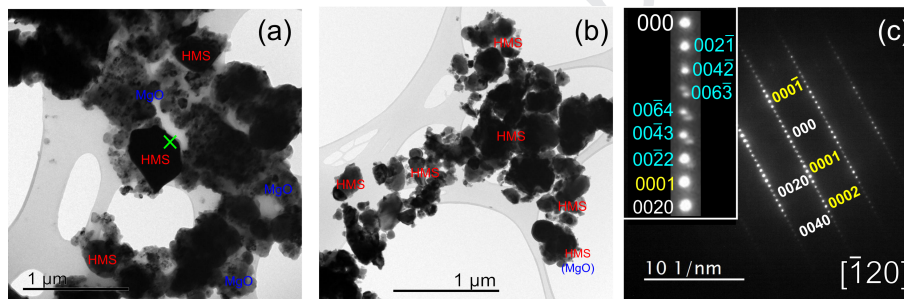


Figure 4: TEM brightfield images of the (a) as-synthesized MR- $\text{MnSi}_\gamma$  + MgO powder and (b) HCl-washed  $\text{MnSi}_\gamma$  powder. Annotations on the images correspond to the main phase deduced from EDS analyses performed on different spots of the observed area. (c) Selected area electron diffraction patterns taken at the green cross in (a) and indexed with the composite crystal structure of  $\text{MnSi}_{1.74}$  described in section 3.3 and pictured in fig.5. For clarity reason, only strong reflections corresponding to the two basic subsystems are indicated along the  $[001]$  row but all satellite reflections could be indexed with  $00\ell m$  indices.  $hk\ell 0$  (white),  $hk0m$  (yellow) and  $hk\ell m$  (blue) Miller indices correspond to the Mn-, Si-subsystems and satellite reflections, respectively. The inset shows a close-up view of the orientation anomaly along the  $[001]$  direction.

### 189 3.3. Structural analysis of the MR- $\text{MnSi}_\gamma$ powders

190  $\text{MnSi}_\gamma$  crystallizes in a composite tetragonal ‘Chimney-Ladder’ structure-type  
 191 - also known as Nowotny phase - in which a ‘ladder’ subsystem of Si-atoms  
 192 ( $P4/nnc$ , no. 126) is penetrating a ‘chimney’ subsystem of Mn ( $I4_1/amd$ , no. 141)  
 193 [35, 36, 37] (fig. 5).

194 As mentioned above, HMS were originally described as a large family of  
 195 stoichiometric compositions with formula  $\text{Mn}_y\text{Si}_x$  where  $x$  and  $y$  are natural

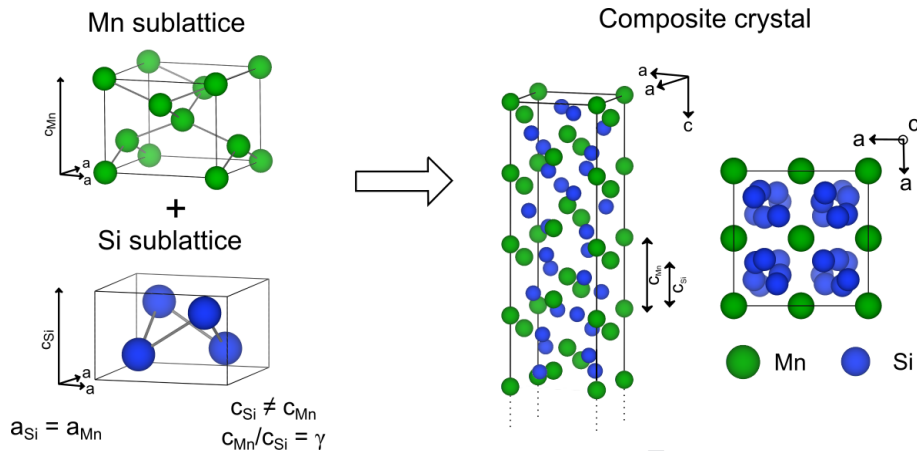


Figure 5: Crystal structure description of  $\text{MnSi}_\gamma$  showing the interpenetrating tetragonal Mn- and Si-subsystems with identical  $a$ - but different  $c$ -lattice parameters (left). The interaction between the two subsystems leads to a composite  $\text{MnSi}_\gamma$  unit-cell (right) where  $\gamma = c_{\text{Mn}}/c_{\text{Si}}$ .

196 numbers and  $\gamma = x/y$  is ranging between  $\approx 1.727$  and 1.75. Accordingly, they  
 197 were described as commensurate structure with  $c$  increasing from 17.4 Å for the  
 198 simplest  $\text{Mn}_4\text{Si}_7$  ( $\gamma = 1.75$ ) to  $c = 117.9$  Å for  $\text{Mn}_{27}\text{Si}_{47}$  ( $\gamma \approx 1.741$ ). Miyazaki  
 199 *et al.* have proposed a more general approach, describing  $\text{MnSi}_\gamma$  as a composite  
 200 structure with a restrained domain of stability for  $\gamma$  [22]. In this approach, the  
 201 structure is composed of two incommensurately modulated subsystems, where  
 202 the modulation results from interactions between mutually incommensurate,  
 203 periodic subsystems [38, 39]. In the case of  $\text{MnSi}_\gamma$ , each subsystem is described  
 204 by only one atom in the asymmetric unit (four equivalent in the basic cell).  
 205 They have identical  $a$  lattice parameters of about 5.53 Å, while the  $c$  lattice  
 206 parameters are different ( $c_{\text{Si}} \approx 2.5$  Å and  $c_{\text{Mn}} \approx 4.4$  Å) with a non-rational ratio  
 207  $\gamma = c_{\text{Mn}}/c_{\text{Si}}$  that corresponds to the Si/Mn stoichiometry of the compound in the  
 208 case of full chemical occupancy.

209 In this context, the 3D lattice periodicity is replaced by a 3D+1 one. The  
 210 symmetry elements present in the structure are described using a  $I4_1/amd(00\gamma)00ss$   
 211 superspace group and four  $hklm$  Miller indices are required for the complete  
 212 indexing of the diffraction patterns [40]. In this superspace description, the re-  
 213 ciprocals basis vectors of the Mn and Si-sublattices in  $\text{MnSi}_\gamma$  are described from

214 the basis vectors of the composite crystal lattice via the W matrices:

$$W_{Mn} = \begin{pmatrix} 1 & 0 & 0 & 0 \\ 0 & 1 & 0 & 0 \\ 0 & 0 & 1 & 0 \\ 0 & 0 & 0 & 1 \end{pmatrix} \quad W_{Si} = \begin{pmatrix} 1 & 0 & 0 & 0 \\ 0 & 1 & 0 & 0 \\ 0 & 0 & 0 & 1 \\ 0 & 0 & 1 & 0 \end{pmatrix} \quad (6)$$

215

216 In this setting, the diffraction patterns of  $MnSi_\gamma$  are composed of  $hk00$ -  
 217 reflections common to both subsystem,  $hkl0$  reflections relative to the basic Mn-  
 218 subsystem,  $hk0m$  reflections relative to the basic Si-subsystem and  $hklm$  satel-  
 219 lite reflections with contribution of the incommensurate modulations. In in-  
 220 commensurately modulated structures, the displacement vector  $u^\mu(x,y,z)$  of the  
 221  $\mu$ -atom relative to its base structure position  $\bar{x}^\mu(x,y,z)$  is described by the mod-  
 222 ulation vector function  $u^\mu(v_\mu)$ . The argument  $v_\mu$  of the modulation function is  
 223 the fourth 3D+1 superspace coordinate of  $\mu$  in the basic structure. From the  
 224 respective W matrices,  $v_{Mn}$  and  $v_{Si}$  are defined by the relations:

$$\begin{aligned} v_{Mn} &= t + \gamma x_3 \\ v_{Si} &= t + 1/\gamma x_4 \end{aligned} \quad (7)$$

225

226 where  $t$  is a real number corresponding to the initial phase of  $u^\mu(v_\mu)$ .

227

228 As the modulation  $u^\mu(v_\mu)$  is periodic in 3D+1 superspace, it can be decom-  
 229 posed by Fourier series according to:

$$u^\mu(v_\mu) = \sum_{k=1}^n A_\mu^k \sin(2\pi k v_\mu) + B_\mu^k \cos(2\pi k v_\mu) \quad (8)$$

230 where the amplitudes  $A_\mu^k$  and  $B_\mu^k$  are refined to fit to the experimental data.

231 The experimental XRD are satisfactorily fitted by Rietveld refinements using

232 this approach as shown *e.g.* in fig. 6a for a HCl-washed  $\text{MnSi}_\gamma$  powder with  
 233 refined lattice parameters, modulation vector and atomic displacement param-  
 234 eters summarized in Table 1 and 2. The refined  $\gamma$  value of 1.7416(2) is in  
 235 agreement with the synthesized and EDS determined compositions, confirming  
 236 the ability of the synthesis technique to produce composition controlled materi-  
 237 als.

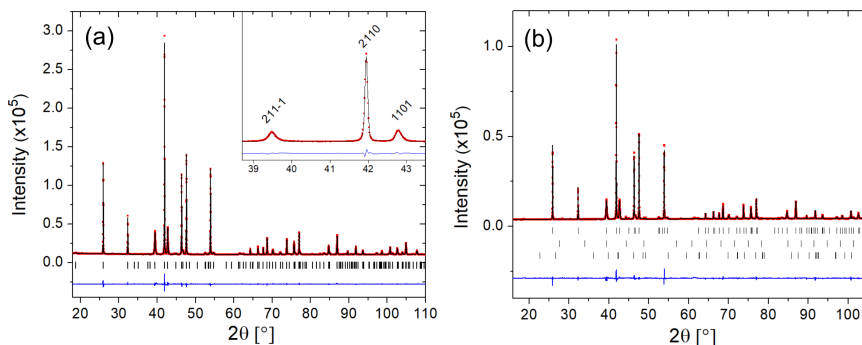


Figure 6: Rietveld refined XRD patterns of (a) washed  $\text{MnSi}_{1.74}$ , with enlarged view in inset, and (b)  $\text{V}_{0.04}\text{Mn}_{0.96}\text{Si}_{1.74}$  powders prepared by magnesioreduction. The experimental data are plotted in red symbols, the calculated one in black line and the difference with a blue line. The vertical ticks indicate the theoretical  $\text{V}_x\text{Mn}_{1-x}\text{Si}_{1.74}$  ( $x = 0, 0.04$ ) Bragg positions up to the 2<sup>nd</sup> order satellite reflections. In (b), the second and third rows indicate the theoretical Bragg positions of  $\text{VSi}_2$  and  $\text{MnSi}$  impurities.

238 In the present case, the collected XRD data allowed satellite reflections up  
 239 to the 2<sup>nd</sup> order to be considered in the refinement procedure as many of them  
 240 were found to have intensities just above the background level. The modulation  
 241 functions were described using Fourier coefficients up to  $n = 2$  and  $n = 4$  for  
 242 Mn and Si subcells, respectively. The large number of refined Fourier coeffi-  
 243 cients used to describe the Si modulation is imposed by the crystal symmetry,  
 244 the first coefficient describing the  $z$  component of the modulation -  $B^4$  - being  
 245 non null for  $n = 4$ . Refined Fourier coefficients are tabulated in Table 2 while  
 246 the resulting modulation functions are plotted in fig. 7. On the one hand, the  
 247 displacement of Mn around its average position  $\bar{x}^{\text{Mn}} = (0,0,0)$  has a small max-  
 248 imum amplitude along  $z$  of about 0.04 Å while no displacement is found in the  
 249  $(x,y)$  plane. On the other hand, Si-atoms at  $\bar{x}^{\text{Si}} = (\frac{1}{4}, \frac{1}{4}, \frac{1}{4})$  show much larger

Table 1: Structural parameters obtained by Rietveld refinement of washed  $\text{MnSi}_{1.74}$  and  $\text{V}_{0.04}\text{Mn}_{0.96}\text{Si}_{1.74}$  XRD patterns.

	$\text{MnSi}_{1.74}$	$\text{V}_{0.04}\text{Mn}_{0.96}\text{Si}_{1.74}$
$\bar{x}^{\text{Mn}} (x,y,z)$	0 0 0 <sup>1</sup>	0 0 0
$a$ (Å)	5.52908(2)	5.5301(1)
Mn $c_{\text{Mn}}$ (Å)	4.36749(4)	4.3696(1)
$\gamma$	1.7416(2)	1.7394(2)
$U_{\text{iso}}$ (Å <sup>2</sup> )	0.0069(8)	0.001(2)
$\bar{x}^{\text{Si}} (x,y,z)$	0.25 0.25 0.25 <sup>1</sup>	0.25 0.25 0.25
$a$ (Å)	5.52908(2)	5.5301(1)
Si $c_{\text{Si}}$ (Å)	2.5077(1) <sup>2</sup>	2.5121(3)
$U_{\text{iso}}$ (Å <sup>2</sup> )	0.0033(4)	0.004(2)

<sup>1</sup> Average position coordinates of Mn and Si are constrained

<sup>2</sup> Calculated as  $c_{\text{Mn}}/\gamma$

250 sinusoidal displacements reaching a maximum of  $x = y \approx 0.2$  Å and  $z \approx 0.08$  Å.  
 251 The large displacement modulations induce the formation of Si-atom helices  
 252 around the  $(\frac{1}{4}, \frac{1}{4}, z)$  axis as shown in the projection of the crystal structure along  
 253 the  $c$ -axis (fig. 5). All these refined values are in very good agreement with  
 254 those reported by Miyazaki *et al.* obtained on high resolution neutron powder  
 255 diffraction data of  $\text{MnSi}_{\approx 1.736}$  synthesized by conventional melting/annealing  
 256 method [22].

Table 2: Refined coefficients of the modulation functions of Mn (top) and Si (bottom) for washed  $\text{MnSi}_{1.74}$  and  $\text{V}_{0.04}\text{Mn}_{0.96}\text{Si}_{1.74}$

	$\text{MnSi}_{1.74}$			$\text{V}_{0.04}\text{Mn}_{0.96}\text{Si}_{1.74}$		
Mn	$x (= x_1)$	$y (= x_2)$	$z (= x_3)$	$x (= x_1)$	$y (= x_2)$	$z (= x_3)$
$B^2$	0	0	-0.019(1)	0	0	-0.017(3)
Si	$x (= x_1)$	$y (= x_2)$	$z (= x_4)$	$x (= x_1)$	$y (= x_2)$	$z (= x_4)$
$A^1$	0.0764(3)	0.0764(3)	0	0.0773(4)	0.0773(4)	0
$B^1$	0.0764(3)	-0.0764(3)	0	0.0773(4)	-0.0773(4)	0
$A^3$	0.0099(6)	0.0099(6)	0	0.0107(7)	0.0107(7)	0
$B^3$	-0.0099(6)	0.0099(6)	0	-0.0107(7)	0.0107(7)	0
$B^4$	0	0	-0.041(3)	0	0	-0.049(4)

257 As illustrated in the inset to fig. 6 with the intense (2110) and (1101) Bragg

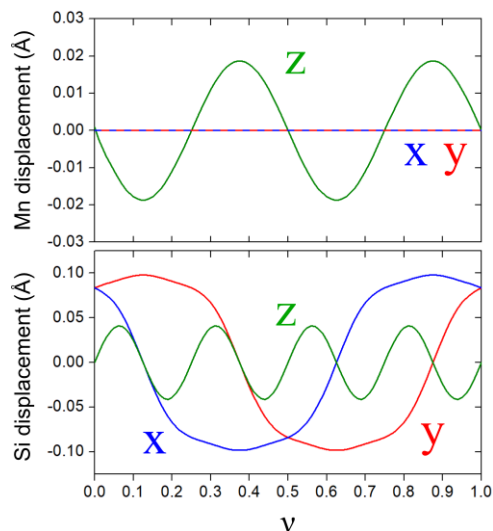


Figure 7: Coordinates of the displacement vector relative to the average position for Mn (top) and Si (bottom) as a function of the fourth space parameter  $v$  for washed  $\text{MnSi}_{1.74}$

258 peaks,  $hk0m$  reflections of the Si subsystem are much broader than the rela-  
 259 tively narrow  $hkl0$  reflections of the Mn subsystem. From the diffractogram  
 260 refinement point of view, this strong peak shape anisotropy between the differ-  
 261 ent families of reflections has been managed using a strain tensor implemented  
 262 in JANA2006. This could be attributed to higher disorder on the Si subsystem  
 263 as confirmed by HRTEM observations that are discussed in next section. This  
 264 strain tensor also avoids the implementation of an extra Si-position in the struc-  
 265 tural model proposed by Akselrud *et al.* to describe the disordered Si-subsystem  
 266 [41].

267 The XRD pattern of washed  $\text{V}_{0.04}\text{Mn}_{0.96}\text{Si}_{1.74}$  powder was also fitted using  
 268 the same approach (fig. 6b, Tables 1 and 2). The lattice parameters are slightly  
 269 larger and  $\gamma$  slightly smaller in the case of the V-doped sample. On the other  
 270 hand, the Fourier coefficient of the modulation functions remains relatively sim-  
 271 ilar. It should be noticed that  $\text{VSi}_2$  and MnSi impurities represent 1 and 2 wt.%  
 272 of the sample, respectively. The presence of  $\text{VSi}_2$  suggest that V was not entirely  
 273 inserted in the structure during the magnesio-reduction process.

### 274 3.4. Microstructure of sintered $\text{MnSi}_\gamma$ pellets

275  $\text{MnSi}_{1.74}$  and  $\text{V}_{0.04}\text{Mn}_{0.96}\text{Si}_{1.74}$  pellets with densities of 96 % according to the  
 276 Archimede weighing were produced by spark plasma sintering. After the sin-  
 277 tering step, both samples are single phase according to XRD (fig. 8 and SI.2),  
 278 indicating that most of the residual  $\text{VSi}_2$  and  $\text{MnSi}$  reacted during the heat treat-  
 279 ment for the doped sample. Accordingly, a significant decrease of  $\gamma$  from about  
 280 1.74 for the as-synthesized MR powder to 1.73 for the as-sintered pellet is ob-  
 281 tained by Rietveld refinements (fig. SI.3), reaching a value close to the arc-  
 282 melted (AM) samples. Generally, the lattice and structural parameters (table  
 283 3) of each composition made by both MR and AM synthesis routes are quite  
 284 equivalent. Upon V-doping, a moderate increase of  $a$  and  $c_{Mn}$  is consistent with  
 285 the slightly larger vanadium metallic radius ( $r_V = 1.346 \text{ \AA}$ ,  $r_{Mn} = 1.264 \text{ \AA}$ [42])  
 286 while a much larger increase of  $c_{Si}$  from about 2.515 to almost 2.53  $\text{ \AA}$  is in  
 287 agreement with Miyazaki's results [20]. As can be seen from the  $2\theta$  shift of the  
 288  $(211\bar{1})$  reflection toward low  $2\theta$  angles, this increase of  $c_{Si}$  is associated to a  
 289 significantly smaller  $\gamma$  value for V-doped samples.

290 Interestingly, the  $(211\bar{1})$  and  $(1101)$  reflections of the AM samples are much  
 291 less affected by the broadening than MR samples. In the case of the MR V-doped  
 292 sample, the  $(1101)$  peak even seems to be composed of three highly convoluted  
 293 peaks. This suggests some level of heterogeneity of  $c_{Si}$  and thus of  $\gamma$  in the MR  
 294 samples, in agreement with similar observations reported by Miyazaki *et al.* in  
 295 V- and Ge-doped HMS prepared by conventional methods [20].

296 EDS mapping on polished surfaces of the SPSed pellets (fig. SI.4) con-  
 297 firms a homogeneous concentration of Mn and Si (within the resolution of the  
 298 technique) on the analyzed areas of the  $\text{MnSi}_{1.74}$  sample, while in the case of  
 299  $\text{V}_{0.04}\text{Mn}_{0.96}\text{Si}_{1.74}$ , a few vanadium-rich areas with diameters below 1  $\mu\text{m}$  could  
 300 be attributed to small amounts of residual  $\text{VSi}_2$  impurity (not visible on XRD  
 301 patterns). As a consequence, the V-concentration in this  $\text{V}_x\text{Mn}_{1-x}\text{Si}_{1.74}$  may be  
 302 slightly below the nominal  $x = 0.04$  value.

303 Residual porosity with average size of approximately 100 nm and located at

304 the grain boundaries is visible for samples prepared by MR and AM syntheses  
 305 (fig. 9). Similar residual porosity after spark plasma sintering is reported in  
 306 samples prepared by other processes such as ball-milling [43], melt-spinning  
 307 [10] or solid-state diffusion [44] and seems thus intrinsic to this material den-  
 308 sified by SPS.

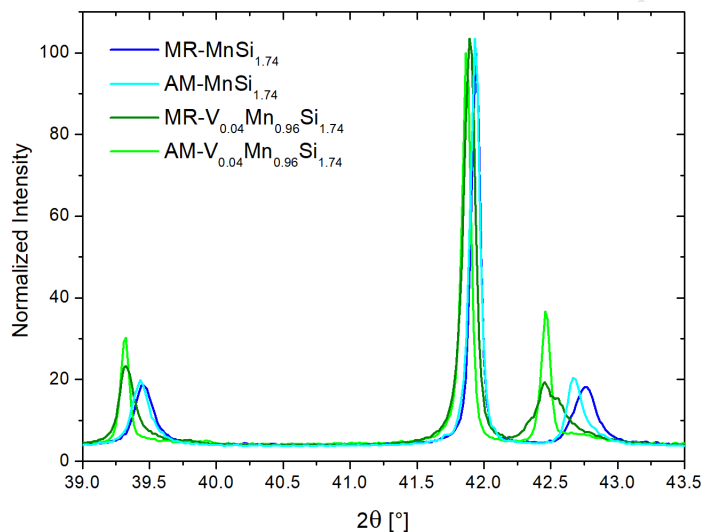


Figure 8: XRD patterns of MR MnSi<sub>1.74</sub> (dark blue), MR V<sub>0.04</sub>Mn<sub>0.96</sub>Si<sub>1.74</sub> (dark green), AM-MnSi<sub>1.74</sub> (bright blue) and AM-V<sub>0.04</sub>Mn<sub>0.96</sub>Si<sub>1.74</sub> (bright green) showing the relative peaks shifts among the samples

309 Further microstructural characterization of the sintered pellets was realized  
 310 by electron back-scattering diffraction (EBSD, fig.9). EBSD maps have been  
 311 obtained by scanning the area with a 50 nm step and by indexing the Kikuchi  
 312 lines using the commensurate Mn<sub>4</sub>Si<sub>7</sub> structure ( $P\bar{4}c2$ ,  $a = 5.52 \text{ \AA}$ ,  $c = 17.46 \text{ \AA}$ ).  
 313 Orientation analysis of the maps do not reveal any crystallographic texturation  
 314 of the pellets which could have been caused by the uniaxial pressing during the  
 315 sintering process [23]. TE properties of the pellets will thus be considered as  
 316 isotropic. The grain size distributions (fig. 9) have been obtained from EBSD  
 317 maps by considering all diffracting domains containing at least 12 pixels (*i.e.*  
 318  $\sim 0.03 \mu\text{m}^2$ ). It follows a log-normal law with average values of 580 nm and  
 319 606 nm for the sintered undoped and V-doped MR samples, respectively. Such

Table 3: Main structural and microstructural characteristics of the SPSeD MR and AM  $V_xMn_{1-x}Si_{1.74}$  ( $x = 0$  and  $0.04$ ) samples used for the TE characterizations

		MR $MnSi_{1.74}$	AM $MnSi_{1.74}$	MR $V_{0.04}Mn_{0.96}Si_{1.74}$	AM $V_{0.04}Mn_{0.96}Si_{1.74}$
	$a$ (Å)	5.5295(3)	5.52954(6)	5.5308(4)	5.5319(1)
	$c_{Mn}$ (Å)	4.3696(3)	4.36834(8)	4.3710(3)	4.3746(1)
	$c_{Si}$ (Å)	2.5156(3)	2.5110	2.5265	2.5291
	$\gamma$	1.7370(3)	1.7397(3)	1.7300(6)	1.7297(1)
Si	$A^1(x)$	0.0768(8)	0.0769(8)	0.0758(8)	0.0753(6)
	$A^2(x)$	0.010(1)	0.013(1)	0.012(1)	0.014(1)
	$A^3(z)$	-0.049(8)	-0.064(7)	-0.042(7)	-0.050(6)
	$U_{iso}^{(2)}$	0.004(3)	0.008(2)	0.001(2)	0.007(2)
Mn	$A^2(z)$	-0.017(4)	-0.009(5)	-0.013(4)	-0.009(3)
	$U_{iso}^{(2)}$	0.001(2)	0.001(1)	0.001(1)	0.001(1)
Impurity (wt. %)	Si	/	2	/	1
	MnSi	/	1	/	1

320 small grain sizes logically lead to a much higher density of grain boundaries  
 321 than a conventionally synthesized AM sample with average grain size estimated  
 322 at  $13 \mu m$  using the same procedure. Enhanced scattering of the phonons at the  
 323 grain boundaries and reduced lattice thermal conductivity are expected from  
 324 such microstructure.

325 Fig. 10a shows a typical low magnification brightfield TEM image of the  
 326 MR  $MnSi_{1.74}$  densified sample. The shape and size distribution of the grains  
 327 are in good agreement with the EBSD analysis. The residual porosity due to  
 328 incomplete densification is confirmed at the grain boundaries. As for the as-  
 329 synthesized powder, no MnSi precipitates are observed inside the grains after  
 330 sintering.

331 As shown on the HRTEM images (fig 10b,c), the great majority of the grain  
 332 boundaries looks well crystalline and free of amorphous layer. Proper sintering  
 333 of nanometric powders can be quite challenging because of oxidation layers or  
 334 residual absorbed species at the surface of the particles which often result in  
 335 much higher electrical resistivity compared to bulk [45]. In the present case,  
 336 the good crystallinity of the grain boundaries is expected to prevent exceed-

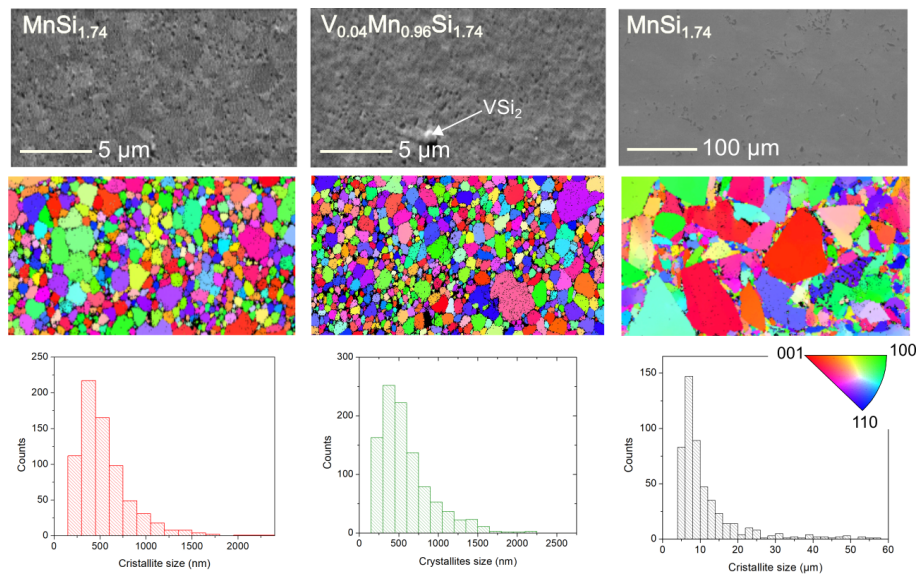


Figure 9: EBSD microstructural analyses of SPSed pellets of MR  $\text{MnSi}_{1.74}$  (left), MR  $\text{V}_{0.04}\text{Mn}_{0.96}\text{Si}_{1.74}$  (middle), and AM  $\text{MnSi}_{1.74}$  (right). The top, middle and bottom rows correspond to backscattered electron images of the analyzed areas, EBSD maps and histograms of the grain size distribution, respectively

337 ingly large decrease of the charge carriers transport while still acting as efficient  
 338 phonon scattering centers.

339 Typical electron diffraction patterns along the  $[\bar{1}20]$  zone axis obtained on  
 340 a MR  $\text{MnSi}_{1.74}$  sintered pellet (fig. 10d) are significantly different than those  
 341 obtained on the as-synthesized powder (fig. 4c). The ‘orientation’ anomalies  
 342 affecting the Si and satellite rows of reflections are no more visible. This evolu-  
 343 tion is attributed to the heat treatment during the sintering and seems correlated  
 344 to the variation of the modulation vector observed by XRD. Such influence of  
 345 the temperature on the microstructural properties of  $\text{MnSi}_\gamma$  have already been  
 346 reported, *e.g.* by Kikuchi *et al.* who reported a linear decrease of  $\gamma$  with tem-  
 347 perature above 770 K associated to a VEC change [46]. In addition, careful  
 348 examination of the diffraction pattern obtained on several areas of the sample  
 349 reveals some degree of structural heterogeneity between different crystals. As  
 350 an example, fig. 10e and 10f are diffraction patterns taken along the  $[\bar{1}10]$  zone  
 351 axis on two different crystals. While in fig. 10e the arrangement of the satellite

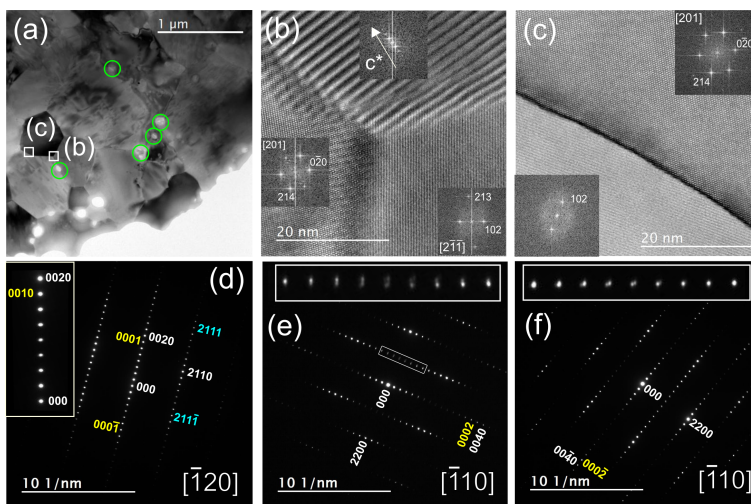


Figure 10: Low magnification brightfield TEM images of typical thinned undoped  $\text{MnSi}_{1.74}$  pellet showing (a) the residual porosity (encircled in green) and the areas chosen for (b) and (c) HRTEM images showing the high crystallinity of the grain boundaries. FFT in insets indicate the crystal orientation of the grains. (d) Typical electron diffraction pattern taken along the  $[\bar{1}20]$  zone axis. (e) and (f) Electron diffraction patterns obtained on two different crystals along the  $[\bar{1}10]$  zone axis showing different anomalies.

352 peaks is equally spaced but slightly misoriented along the  $c$ -axis, fig. 10f shows  
 353 on the contrary a split in satellite spot position in agreement with a variation of  
 354 the modulation vector. A clear explanation of the origin of such microstructural  
 355 effects is not available in literature and moreover out of the scope of the present  
 356 work. However it is worth to underline that such effects are not homogeneous  
 357 at the micrometer scale throughout the samples and are a characteristic of HMS  
 358 that should be taken into account during theoretical modeling of the system.

359 An important contrast inside the crystals can be observed in brightfield mode  
 360 (fig. 10a) and are attributed to local deviations from the diffraction condition  
 361 due to large lattice distortions. Magnified images of this area are shown in fig.  
 362 11a and 11b revealing high concentration of dislocation-like defects propagat-  
 363 ing lattice distortion up to a distance of 50 nm in the crystal. A more detailed  
 364 study of lattice defects was realized by high resolution imaging on thin crystals  
 365 oriented along the  $[\bar{1}20]$  zone axis. A defect-free area is shown in fig. 11(c)  
 366 revealing two types of structural features: (i) large fringes with approximately

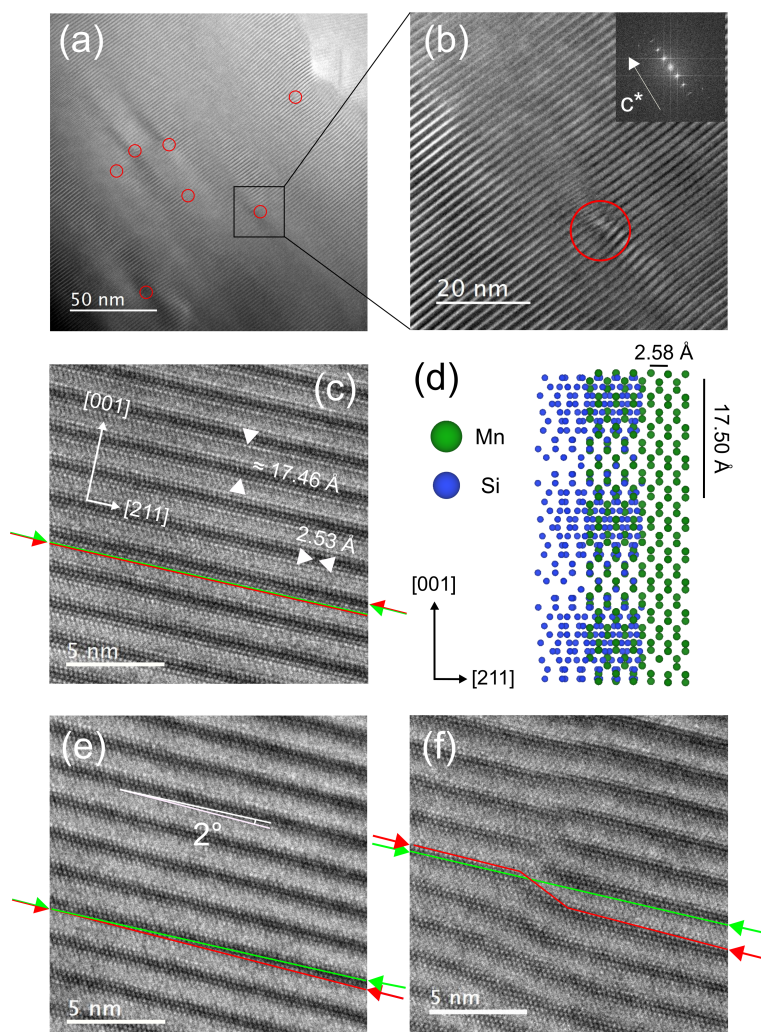


Figure 11: (a) and (b) Brightfield images of MR  $\text{MnSi}_{1.74}$  sintered pellet showing dislocation-like defects (encircled in red) at two different magnifications. (c) Typical HRTEM image of a defect-free area of a  $\text{MnSi}_{1.74}$  crystal taken along the  $[\bar{1}20]$  zone axis with average characteristic distances of the lattice determined from the corresponding FFT image. The orientations of the Moiré fringes and the Mn atomic rows are emphasized on the images with red and green lines, respectively. (d) Scheme of the formation of Moiré-like fringes along the  $[\bar{1}20]$  direction by interaction of the Si-sublattice (left side) and Mn-sublattice (right side). (e) and (f) HRTEM images showing the tilting of the Moiré fringes relative to the  $[211]$  direction and a dislocation-like defect, respectively.

367 17.46 Å periodicity along the  $[001]$  direction corresponding to the  $c$ -axis of the  
 368 commensurate structure of  $\text{Mn}_4\text{Si}_7$  and generated by Moiré interferences be-  
 369 tween the two Mn- and Si-subsystems of the composite crystal and (ii) atomic

370 rows spaced by approximately 2.53 Å along the [211] direction and correspond-  
371 ing to the Mn-Mn distance in the  $[\bar{1}20]$  projection of the structure (fig. 11c).  
372 The schematic representation of the crystal structure projection along the  $[\bar{1}20]$   
373 direction illustrates the formation of the Moiré fringes by interaction of the two  
374 sublattices (fig. 11c). As assumed by the structural model, the orientation of the  
375 Moiré fringes and the Mn rows are both parallel to the [211] direction because  
376 of the existence of lattice translation symmetry in the (001) plane. Surpris-  
377 ingly, the situation is somewhat different in fig. 11e taken in a different area  
378 of the same crystal, where the Moiré fringes are found to be tilted by about  
379  $2^\circ$  with respect to the Mn row itself. Ye and Amelinckx reported similar ob-  
380 servations and explained it as a small systematic ‘phase-shift’ of the Si helical  
381 arrangement inside the columnar Mn-sublattice resulting in the tilting of the  
382 Moiré fringes [34]. According to these authors, the loss of the tetragonal sym-  
383 metry in the area of the crystal affected by the Si helices ‘phase-shift’ explains  
384 the ‘orientation’ anomalies visible on the electron diffraction patterns. Similar  
385 type of images taken on the dislocation-like defects (fig. 11f) reveals that only  
386 the Moiré fringes are deformed on these areas of the crystal. As shown by the  
387 green line, the Mn rows remains well oriented and defect-free throughout the  
388 analyzed area and even close to the lattice defect where severe distortion is ex-  
389 pected. From these observations, the Si sublattice can be described as highly  
390 deformed by numerous defects while on the contrary the Mn lattice remains  
391 well crystallized and less affected by Si sublattice disorder. It should be noticed  
392 that this more ‘realistic’ description of the HMS structure is consistent with the  
393 peak shape broadening of the Si  $hk0m$  reflections clearly visible on the powder  
394 XRD patterns and supports the use of the strain tensor applied in our Rietveld  
395 refinements.

396 The presence of numerous defects and heterogeneities within the submi-  
397 cronous grains of MR  $\text{MnSi}_{1.74}$  might act as efficient scattering centers for phonons  
398 and thus might strongly influence the thermal conductivity of the materials.  
399 In the next section, the thermoelectric properties of pristine and V-doped MR  
400  $\text{MnSi}_{1.74}$  are thus presented and compared to conventionally synthesized AM

401 counterparts. The objective is to discuss the effect of the different synthesis  
 402 routes and microstructures on the TE properties of comparable polycrystalline  
 403  $\text{MnSi}_{1.74}$  samples.

### 404 **3.5. Thermoelectric properties of MR and AM $\text{MnSi}_{1.74}$ and** 405 **$\text{V}_{0.04}\text{Mn}_{0.96}\text{Si}_{1.74}$**

406 The TE properties of  $\text{MnSi}_{1.74}$  and  $\text{V}_{0.04}\text{Mn}_{0.96}\text{Si}_{1.74}$  synthesized by magnesio-re-  
 407 duction or arc-melting were measured from room temperature up to 800 K (fig.  
 408 12). Measurements of the electronic properties were cycled twice and showed  
 409 good reversibility within a time span of few hours at high temperature.

410 The electrical resistivity of MR  $\text{MnSi}_{1.74}$  (fig. 12a) increases from  $23 \mu\Omega\cdot\text{m}$   
 411 at 320 K to  $39 \mu\Omega\cdot\text{m}$  at 750 K, in agreement with the behavior expected for a  
 412 heavily degenerated semiconductor. In the same temperature range, its positive  
 413 Seebeck coefficient (fig. 12b) increases accordingly from 135 to  $230 \mu\text{V}\cdot\text{K}^{-1}$ .  
 414 The electronic properties of AM  $\text{MnSi}_{1.74}$  were measured in the same conditions:  
 415 at room temperature, the electrical resistivity and Seebeck coefficient are found  
 416 to be 17 % and 2 % lower for the AM  $\text{MnSi}_{1.74}$  sample in comparison to MR  
 417 sample. At higher temperature, the difference in electrical resistivity becomes  
 418 less and less significant, which is attributed to the apparition of the bipolar effect  
 419 arising at slightly lower temperature (700-750 K) in the case of the MR sample.  
 420 This effect corresponds to the thermal activation of minor carriers across the  
 421 band gap (electrons in this case) leading to the simultaneous decrease of the  
 422 electrical resistivity and the Seebeck coefficient. Maximum power factor  $PF$  of  
 423  $1.3 \text{ mW m}^{-1} \text{ K}^{-2}$  at 740 K and  $1.4 \text{ mW m}^{-1} \text{ K}^{-2}$  at 700 K (fig. 12c) are found  
 424 for MR and AM  $\text{MnSi}_{1.74}$ , respectively. This corresponds to a 5 % reduction  
 425 of the maximum  $PF$  which can be attributed in a large extent to the higher  
 426 resistivity of the MR sample. Assuming similar charge carrier concentration in  
 427 MR and AM samples from equivalent Seebeck coefficients and  $\gamma$ -value [46], the  
 428 higher electrical resistivity in the mesostructured samples could be explained  
 429 both by its lower density and possibly by higher scattering of charge carriers at  
 430 the numerous grain boundaries.

431 Fig. 12d shows the temperature dependence of the total  $\kappa_{tot}(T)$  and lattice  
 432  $\kappa_L(T)$  thermal conductivities calculated by subtracting to  $\kappa_{tot}(T)$  the electronic  
 433 contribution  $\kappa_e(T)$  calculated using the Wiedemann-Franz law  $\kappa_e(T) = L T/\rho(T)$   
 434 with  $L = 2.4 \cdot 10^{-8} \text{ W } \Omega \text{ K}^{-2}$ . The lattice thermal conductivity of MR  $\text{MnSi}_{1.74}$   
 435 amounts to  $2.3 \text{ W m}^{-1} \text{ K}^{-1}$  at 320 K, which corresponds to a 13 % decrease  
 436 compared to AM  $\text{MnSi}_{1.74}$  at the same temperature. The beneficial reduction of  
 437 the lattice thermal conductivity in MR  $\text{MnSi}_{1.74}$  is attributed to the smaller grain  
 438 sizes and the high concentration of defects as evidenced by EBSD and TEM  
 439 analyses. However, the effect of mesostructuration becomes less and less effi-  
 440 cient with increasing temperature and the lattice thermal conductivities of the  
 441 two samples ultimately reach similar value at 750 K corresponding to the tem-  
 442 perature with the highest  $PF$ . Equivalent maximum  $ZT$  of about 0.4 is achieved  
 443 at 750 K which is in good agreement with the best performances reported for  
 444 undoped HMS synthesized by conventional melting/annealing/SPS [47, 48].  
 445 No improvement of the  $ZT$  could be achieved because the beneficial effect of  
 446 the mesostructuration on  $\kappa_{tot}$  is counterbalanced by the deterioration of  $PF$  re-  
 447 sulting in equivalent  $ZT$  values over the whole temperature range. Concordant  
 448 experimental results show that highly-densified nanostructured HMS (average  
 449 grain size around 200 nm) synthesized by ball milling followed by SPS did not  
 450 improve the  $ZT$  also because of the drop of the power factor [9]. It suggests that  
 451 any attempt to reduce the grain size down to few hundreds of nm is inefficient  
 452 to improve  $ZT$  in the case of  $\text{MnSi}_{1.74}$ .

453 Increasing  $PF$  of MR-HMS was attempted by partially substituting manganese  
 454 with vanadium up to 4 %. Vanadium-doping was reported to effectively im-  
 455 proved the power factor of  $\text{MnSi}_\gamma$  while employing a relatively abundant el-  
 456 ement compared to other commonly used dopant such as Ge or Re [49]. In  
 457 addition,  $\text{V}_2\text{O}_5$  can be reduced relatively easily by Mg in the synthesis condi-  
 458 tion unlike other very stable oxides such as  $\text{Al}_2\text{O}_3$ . As for undoped  $\text{MnSi}_{1.74}$ , TE  
 459 measurements were realized on both MR and AM  $\text{V}_{0.04}\text{Mn}_{0.96}\text{Si}_{1.74}$ . The elec-  
 460 trical resistivity and the Seebeck coefficient of both samples decrease with the  
 461 insertion of vanadium in the structure. This is consistent with an increase of

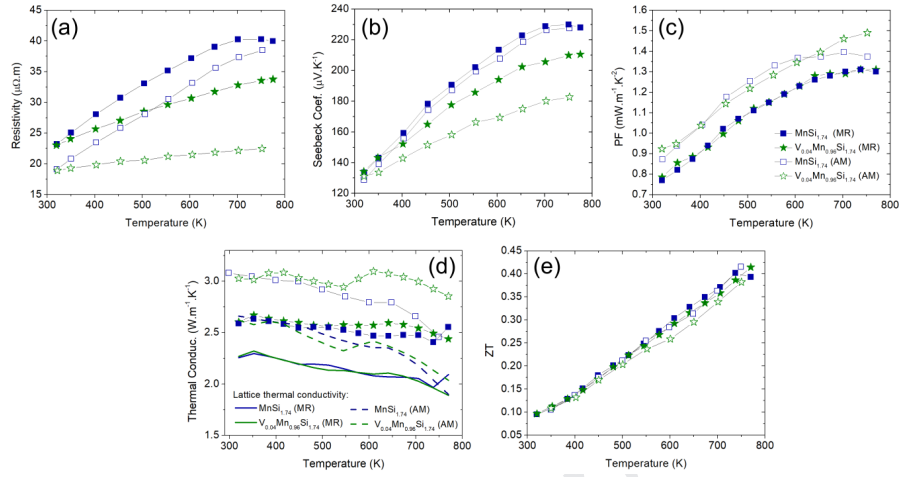


Figure 12: High temperature thermoelectric properties of  $MnSi_{1.74}$  (blue squares) and  $V_{0.04}Mn_{0.96}Si_{1.74}$  (green stars) synthesized by magnesioreduction (MR, filled symbols) and conventional arc-melting (AM, empty symbols): thermal dependence of (a) electrical resistivity, (b) thermopower, (c) power factor, (d) total (symbols) and lattice (solid lines for MR  $MnSi_{1.74}$  and dotted lines for AM  $MnSi_{1.74}$ ) thermal conductivities and (e) resulting figure-of-merit.

462 the holes concentration in the materials resulting from the substitution of Mn  
 463 by an electron-poorer element. The less pronounced effect of the doping on the  
 464 MR sample could be explained by the probable smaller amount of V effectively  
 465 substituting Mn due to the residual  $VSi_2$  precipitates observed by EDS mapping.  
 466 Miyazaki *et al.* [49] clearly showed a linear increase of the charge carrier con-  
 467 centration with V-doping. Accordingly, a slightly smaller charge carrier density  
 468 is expected in the MR-sample, also in agreement with the higher Seebeck co-  
 469 efficient of this material. Consequently, doping the MR sample do not improve  
 470  $PF$  while for the AM sample it leads only to a small improvement of about 8 %  
 471 above 700 K. Similarly, doping do not induce significant improvement of the  
 472 lattice thermal conductivity which remain identical to the undoped sample over  
 473 the whole temperature range. Neither the mass fluctuation scattering of thermal  
 474 phonons at the disordered Mn/V sites, nor the submicrometric  $VSi_2$  precipitates  
 475 present in the materials seem to significantly influence  $\kappa_L$ . As a consequence,  
 476 no improvement of  $ZT_{max}$  has been achieved in our case by vanadium doping.

## 477 **4. Conclusion**

478 A new magnesio-reduction synthesis for high purity  $\text{MnSi}_{1.74}$  is reported. This  
479 method offers many advantages over conventional melting/annealing syntheses  
480 such as the use of cheap and air-stable precursors (MnO and Si), relatively fast  
481 heat treatment at moderate temperature and the possibility to produce doped  
482 compounds. Additionally, a finely divided powder is directly obtained, which is  
483 suitable for the sintering of mesostructured materials with average grain size of  
484 about 500 nm. The influence of the microstructure, investigated by means of  
485 EBSD and TEM, on the thermoelectric properties was evaluated by comparison  
486 with a sample synthesized by a conventional arc-melting/annealing/sintering  
487 process and composed of much larger grains. The thermal conductivity is de-  
488 creased by up to 25% at 300 K thanks to the mesostructuration and associated  
489 crystal defect density. However, this beneficial effect is counterbalanced by a de-  
490 crease of the power factor, resulting eventually in materials with similar  $ZT_{max} \simeq$   
491 0.4 at 750 K. The present results suggest that microstructure engineering alone  
492 might not be a sufficient strategy to improve the TE properties of HMS.

## 493 **Acknowledgements**

494 Francis Gouttefangeas is acknowledged for SEM images and EDS analyses per-  
495 formed on the CMEBA platform. TEM experiments were performed on THEMIS  
496 platform. Both platforms belong to the ScanMAT unit (UMS 2001, Univer-  
497 sity of Rennes 1) which received a financial support from the European Union  
498 (CPER-FEDER 2007-2014). The authors acknowledge support from CREST JP-  
499 MJCR15Q6 and JSPS KAKENHI JP17H02749, JP16H06441.

## 500 **References**

- 501 [1] L. E. Bell, Cooling, heating, generating power, and recovering waste heat  
502 with thermoelectric systems, *Science* 321 (2008) 1457–1461.
- 503 [2] I. Petsagkourakis, K. Tybrandt, X. Crispin, I. Ohkubo, N. Satoh, T. Mori,

- 504 Thermoelectric materials and applications for energy harvesting power  
505 generation, *Sci. Technol. Adv. Mater.* 19 (2018) 836–862.
- 506 [3] L. Aixala, C. de Vault, Waste heat recovery by thermoelectricity on pas-  
507 senger car and heavy-duty truck diesel engine: the RENOTER project, 3<sup>rd</sup>  
508 Thermoelectrics Applications Workshop Baltimore, USA (2012) –.
- 509 [4] G. Skomedal, L. Holmgren, H. M. and I.S. Eremin, G. Isachenko, M. Jae-  
510 gle, K. Tarantik, N. Vlachos, M. Manoli, T. Kyratsi, D. Berthebaud, N. Y. D.  
511 Truong, F. Gascoin, Design, assembly and characterization of silicide-  
512 based thermoelectric modules, *Energy Convers. Manag.* 110 (2016) 13–  
513 21.
- 514 [5] T. Mori, Novel principles and nanostructuring methods for enhanced ther-  
515 moelectrics, *Small* 13 (2017) 1702013.
- 516 [6] J. Mao, Z. Liu, J. Zhou, H. Zhu, Q. Zhang, G. Chen, Z. Ren, Advances in  
517 thermoelectrics, *Adv. Phys.* 67 (2018) 69–147.
- 518 [7] D. N. Truong, D. Berthebaud, F. Gascoin, H. Kleinke, Molybdenum, tung-  
519 sten, and aluminium substitution for enhancement of the thermoelectric  
520 performance of higher manganese silicides, *J. Electron. Mater.* 44 (2015)  
521 3603–3611.
- 522 [8] V. Ponnambalam, D. T. Morelli, Effect of addition of the elements Cr, V,  
523 Mo, Ge, Re and Ru on the thermoelectric properties of higher manganese  
524 silicides  $\text{MnSi}_{\sim 1.74}$ , *Mater. Res. Express* 6 (2018) 025507.
- 525 [9] X. Chen, L. Shi, J. Zhou, J. B. Goodenough, Effects of ball milling on mi-  
526 crostructures and thermoelectric properties of higher manganese silicides,  
527 *J. Alloys Compd.* 641 (2015) 30–36.
- 528 [10] S. Muthiah, R. C. Singh, B. D. Pathak, P. K. Avasthi, R. Kumar, A. Kumar,  
529 A. K. Srivastava, A. Dhar, Significant enhancement in thermoelectric per-  
530 formance of nanostructured higher manganese silicides synthesized em-  
531 ploying a melt spinning technique, *Nanoscale* 10 (2018) 1970–1977.

- 532 [11] W. Luo, H. Li, F. Fu, W. Hao, X. Tang, Improved Thermoelectric Properties  
533 of Al-Doped Higher Manganese Silicide Prepared by a Rapid Solidification  
534 Method, *J. Electron. Mater.* 40 (2011) 1233–1237.
- 535 [12] X. She, X. Su, H. Du, T. Liang, G. Zheng, Y. Yan, R. Akram, C. Uher, X. Tang,  
536 High thermoelectric performance of higher manganese silicides prepared  
537 by ultra-fast thermal explosion, *J. Mater. Chem. C* 3 (2015) 12116–12122.
- 538 [13] Y. Thimont, L. Presmanes, V. Baylac, P. Tailhades, D. Berthebaud, F. Gas-  
539 coin, Thermoelectric higher manganese silicides: synthesized, sintered  
540 and shaped simultaneously by selective laser sintering/melting additive  
541 manufacturing technique, *Mater. Lett.* 214 (2018) 236–239.
- 542 [14] S. Vivès, C. Navone, E. Gaudin, S. Gorsse, Improved microstructure and  
543 thermoelectric properties of higher manganese silicide processed by reac-  
544 tive spark plasma sintering, *J. Mater. Sci.* 52 (2017) 12826–12833.
- 545 [15] A. Yamamoto, S. Ghodke, H. Miyazaki, M. Inukai, Y. Nishino, M. Mat-  
546 sunami, T. Takeuchi, Thermoelectric properties of supersaturated Re solid  
547 solution of higher manganese silicides, *Jpn. J. Appl. Phys.* 55 (2016)  
548 020301.
- 549 [16] T. Homma, T. Kamata, N. Saito, S. Ghodke, T. Takeuchi, Effects of Re  
550 substitution for Mn on microstructures and properties in Re-substituted  
551 higher manganese silicide thermoelectric material, *J. Alloys Compd.* 776  
552 (2019) 8–15.
- 553 [17] A. Berche, E. Ruiz-Théron, J.-C. Tedenac, R. Ayrat, F. Rouessac, P. Jund,  
554 Thermodynamic description of the Mn-Si system: an experimental and  
555 theoretical work, *J. Alloys Compd.* 615 (2014) 693–702.
- 556 [18] W. M. Haynes, D. R. Lide, T. J. Bruno, *CRC Handbook of Chemistry and*  
557 *Physics*, CRC Press Ed. (2015-2016) 6–91.

- 558 [19] S. N. Girard, X. Chen, F. Meng, A. Pokhrel, J. Zhou, L. Shi, S. Jin, Ther-  
559 moelectric properties of undoped high purity higher manganese silicides  
560 grown by chemical vapor transport, *Chem. Mater.* 26 (2014) 5097–5104.
- 561 [20] Y. Miyazaki, H. Hamada, K. Hayashi, K. Yubuta, Crystal structure and Ther-  
562 moelectric Properties of Lightly Vanadium-Substituted Higher Manganese  
563 Silicides  $Mn_{(1-x)}V_xSi_\gamma$ , *J. Electron. Mater.* 46 (2017) 2705–2709.
- 564 [21] S. S. Ravazi-Tousi, Y.-C. Tseng, Failure analysis and mechanical reliability  
565 of cast higher manganese silicide, *J. Alloys Compd.* 764 (2018) 745–754.
- 566 [22] Y. Miyazaki, D. Igarashi, K. Hayashi, T. Kajitani, K. Yubuta, Modulated  
567 crystal structure of chimney-ladder higher manganese silicides  $MnSi_\gamma$   
568 ( $\gamma \approx 1.74$ ), *Phys. Rev. B* 78 (2008) 214104.
- 569 [23] Y. Sadia, Z. Aminov, D. Mogilyansky, Y. Gelbstein, Texture anisotropy of  
570 higher manganese silicide following arc-melting and hot-pressing, *Inter-  
571 metallics* 68 (2016) 71–77.
- 572 [24] S. Le Tonquesse, E. Alleno, V. Demange, V. Dorcet, L. Joanny, C. Prestipino,  
573 O. Rouleau, M. Pasturel, Innovative One-step Synthesis of Mesostructured  
574  $CoSb_3$ -based Skutterudites by Magnesio-reduction, *J. Alloys Compd.* 796  
575 (2019) 176.
- 576 [25] S. N. Girard, T. J. Slade, X. Chen, F. Meng, L. Shi, S. Jin, Nanostructured  
577 higher manganese silicides synthesized by magnesio-reduction in molten  
578 salt fluxes, Abstract book of the 33<sup>th</sup> International Conference on Ther-  
579 moelectrics Nashville, USA.
- 580 [26] V. Petříček, M. Dušek, L. Palatinus, Crystallographic Computing System  
581 JANA2006: General features, *Z. Kristall.* 229 (2014) 345–352.
- 582 [27] H. J. T. Ellingham, Reducibility of oxides and sulfides in metallurgical  
583 processes, *J. Soc. Chem. Ind.* 65 (1944) 125–160.

- 584 [28] O. Knacke, O. Kubaschewski, K. Hesselmann, Thermo-chemical Properties  
585 of Inorganic Substances, Springer Ed. vol. II (1991) –.
- 586 [29] Z. Zamanipour, X. Shi, M. Mozafari, J. S. Krasinski, L. Tayebi, D. Vashae,  
587 Synthesis, characterization, and thermoelectric properties of nanostruc-  
588 ture bulk p-type  $\text{MnSi}_{1.73}$ ,  $\text{MnSi}_{1.75}$ , and  $\text{MnSi}_{1.77}$ , *Ceram. Int.* 39 (2013)  
589 2353–2358.
- 590 [30] M. Saleemi, A. Famengo, S. Fiameni, S. Boldrini, S. Battiston, M. Johns-  
591 son, M. Muhammed, M. Toprak, Thermoelectric performance of higher  
592 manganese silicide nanocomposites, *J. Alloys Compd.* 619 (2015) 31–37.
- 593 [31] Y. Sadia, L. Dinnerman, Y. Gelbstein, Mechanical alloying and spark  
594 plasma sintering of higher manganese silicides for thermoelectric appli-  
595 cations, *J. Electron. Mater.* 42 (2013) 1926–1931.
- 596 [32] C. Won, H. Nersisyan, H. Won, Titanium powder prepared by a rapid  
597 exothermic reaction, *Chem. Eng. J.* 157 (2010) 270–275.
- 598 [33] H. Nersisyan, H. Won, C. Won, A. Joc, J. Kim, Direct magnesio-reduction  
599 of titanium dioxide to titanium powder through combustion synthesis,  
600 *Chem. Eng. J.* 235 (2014) 67–74.
- 601 [34] H. G. Ye, S. Amelinckx, High-resolution electron microscopic study of man-  
602 ganese silicides  $\text{MnSi}_{2-x}$ , *J. Solid State Chem.* 61 (1986) 8–39.
- 603 [35] O. Schwomma, H. Nowotny, A. Wittmann, Die Kristallarten  $\text{RuSi}_{1.5}$ ,  
604  $\text{RuGe}_{1.5}$  und  $\text{MnSi}_{1.7}$ , *Monatsh. Chem.* 94 (1963) 681–685.
- 605 [36] G. Flieher, H. Völlenkle, H. Nowotny, Crystal structure of  $\text{Mn}_{15}\text{Si}_{26}$  (man-  
606 ganese silicides of  $\text{Mn}_n\text{Si}_{2n-m}$  type, *Monatsh. Chem.* 98 (1967) 2173–  
607 2179.
- 608 [37] H. Knott, M. Mueller, L. Heaton, Crystal structure of  $\text{Mn}_{15}\text{Si}_{26}$ , *Acta Crys-*  
609 *tallogr.* 23 (1967) 549–555.

- 610 [38] S. van Smaalen, Symmetry of composite crystals, *Phys. Rev. B* 43 (1991)  
611 11330–11341.
- 612 [39] V. Petricek, K. Maly, P. Coppens, X. Bu, I. Cisarova, A. Frost-Jensen, The de-  
613 scription and analysis of composite crystals, *Acta Crystallogr. A* 47 (1991)  
614 210–216.
- 615 [40] P. M. D. Wolff, T. Janssen, A. Janner, The superspace groups for incom-  
616 mensurate crystal-structures with a one-dimensional modulation, *Acta*  
617 *Crystallogr. A* 37 (1981) 625–636.
- 618 [41] L. Akselrud, R. C. Gil, M. Wagner-Reetz, Y. Grin, Disorder in the composite  
619 crystal structure of the manganese ‘disilicide’  $\text{MnSi}_{1.73}$  from powder X-ray  
620 diffraction data, *Acta Crystallogr. B* 71 (2015) 707–712.
- 621 [42] E. Teatum, K. Gschneidner, J. Waber, Compilation of calculated data use-  
622 ful in predicting metallurgical behaviour of the elements in binary alloy  
623 systems, Los Alamos Scientific Laboratory LA-2345 (1960) –.
- 624 [43] Y.-G. Lee, M.-K. Choi, I.-H. Kim, S.-C. Ur, Thermoelectric properties of  
625 Nowotny phase, higher manganese silicides synthesized by mechanical  
626 alloying process, *J. Ceram. Process. Res.* 13 (2012) 816–819.
- 627 [44] X. Chen, A. Weathers, D. Salta, L. Zhang, J. Zhou, J. B. Goodenough,  
628 L. Shi, Effects of (Al,Ge) double doping on the thermoelectric properties  
629 of higher manganese silicides, *J. Appl. Phys.* 114 (2013) 173705.
- 630 [45] A. Khan, M. Saleemi, M. Johnsson, L. Han, N. Nong, M. Muhammed,  
631 M. Toprak, Fabrication, spark plasma consolidation, and thermoelectric  
632 evaluation of nanostructured  $\text{CoSb}_3$ , *J. Alloys Compd.* 612 (2014) 293–  
633 300.
- 634 [46] Y. Kikuchi, T. Nakajo, K. Hayashi, Y. Miyazaki, High temperature X-ray  
635 diffraction study on incommensurate composite crystal  $\text{MnSi}_\gamma$  - (3+1)-  
636 dimensional superspace approach, *J. Alloys Compd.* 616 (2014) 263–267.

- 637 [47] W. Luo, H. Li, Y. Yan, Z. Lin, X. Tang, Q. Zhang, C. Uher, Rapid synthesis  
638 of high thermoelectric performance higher manganese silicide with in-situ  
639 formed nano-phase of MnSi, *Intermetallics* 19 (2011) 404–408.
- 640 [48] T.-H. An, S.-M. Choi, W.-S. Seo, C. Park, I.-H. Kim, S.-U. Kim, The effect of  
641 microstructure on the thermoelectric properties of polycrystalline Higher  
642 Manganese Silicides, *Jpn. J. Appl. Phys.* 52 (2013) 10MC11.
- 643 [49] Y. Miyazaki, H. Hamada, H. Nagai, K. Hayashi, Crystal Structure and Ther-  
644 moelectric Properties of Lightly Substituted Higher Manganese Silicides,  
645 *Materials* 11 (2018) 926.

- Mesosstructured higher manganese silicides are synthesized by magnesioreduction
- Crystal structures are refined in composite-incommensurate unit-cells
- Microstructures are examined by EBSD and TEM
- The decrease in thermal conductivity is correlated to the microstructure

Journal Pre-proof